Effects of liquid water injection on flame surface topology and propagation characteristics in spray flames: A direct numerical simulation analysis

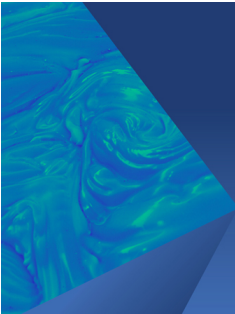R. Concetti ✉ iD ; J. Hasslberger iD ; N. Chakraborty iD ; M. Klein iD

Check for updates

View Online

Export Citation

Physics of Fluids

Special Topic:

John Michael Dealy (1937-2024): Celebrating His Life

Guest Editors: Alan Jeffrey Giacomin and Savvas G. Hatzikiriakos

Submit Today!

AIP Publishing

AIP Publishing

Effects of liquid water injection on flame surface topology and propagation characteristics in spray flames: A direct numerical simulation analysis

View Online   Export Citation   CrossMark

R. Concetti,[1,a] (iD) J. Hasslberger,[1] (iD) N. Chakraborty,[2] (iD) and M. Klein[1] (iD)

AFFILIATIONS

[1]Department of Aerospace Engineering, University of the Bundeswehr Munich, Werner-Heisenberg-Weg 39, 85577 Neubiberg, Germany

[2]School of Engineering, Newcastle University, Claremont Road, Newcastle NE1 7RU, United Kingdom

[a]Author to whom correspondence should be addressed: riccardo.concetti@unibw.de

ABSTRACT

The effects of water injection on flame surface topology and local flame propagation characteristics have been analyzed for statistically planar turbulent n-heptane spray flames with an overall (i.e., liquid + gaseous) equivalence ratio of unity using carrier-phase direct numerical simulations. Most fuel droplets have been found to evaporate as they approach the flame even though some droplets can survive until the burnt gas side is reached, whereas water droplets do not significantly evaporate ahead of the flame and the evaporation of water droplets starts to take place in the reaction zone and is completed within the burnt gas. However, the gaseous-phase combustion occurs predominantly in fuel–lean mode although the overall equivalence ratio remains equal to unity. The water injection has been found to suppress the fuel droplet-induced flame wrinkling of the progress variable isosurface under the laminar condition, and this effect is particularly strong for small water droplets. However, turbulence-induced flame wrinkling masks these effects, and thus, water injection does not have any significant impact on flame wrinkling for the turbulent cases considered here. The higher rate of evaporation and the associated high latent heat extraction for smaller water droplets induce stronger cooling effects, which weakens the effects of chemical reaction. This is reflected in the decrease in the mean values of density-weighted displacement speed with decreasing water droplet diameter. The weakening of flame wrinkling as a result of injection of small water droplets is explained through the curvature dependence of the density-weighted displacement speed. The combined influence of cooling induced by the latent heat extraction of water droplets and flame surface flattening leads to a decrease in volume-integrated burning rate with decreasing water droplet diameter in the laminar cases, whereas the cooling effects are primarily responsible for the drop in burning rate with decreasing water droplet diameter in the turbulent cases.

I. INTRODUCTION

Injection of water droplets is often employed for fire abatement,[1] explosion mitigation,[2,3] and in gas turbines for power boosting and reduction of pollutant emissions.[4] For example, the power output of the BMW M4 GTS engine can be increased,[4] and the power output for gas turbines can potentially be augmented by 30% by water injection.[4] The Water Boost system by Bosch offers a reduction in CO_2 emission and an increase in fuel economy.[4] Furthermore, the decrease in temperature resulting from liquid-phase evaporation impacts the formation of NO_x through a significant inhibition of the Zeldovich mechanism, which is responsible for nitrogen oxide generation at elevated temperatures.[5] Despite these advantageous features of water

injection, the influence of water injection in flames has not been analyzed sufficiently in the existing literature. The effects of water injection on turbulent premixed flames depend on the ratios of the vaporization timescale of droplets and the chemical timescale (i.e., evaporation Damköhler number) and the ratio of inter-droplet distance to the flame thickness.[6–8] The influence of water droplets on premixed flames in terms of either flame quenching or power boosting depends on these two non-dimensional quantities. In discerning the predominant effect, whether it be the cooling influence or the evaporation-induced wrinkling of the flame surface, which potentially can lead to an enhancement in the burning rate, the aforementioned non-dimensional parameters alongside flame topology play a pivotal role.

The evaporation Damköhler number assumes small values for small droplet sizes because of their small evaporation time.[6–9] For a given water mass loading, a decrease in droplet diameter reduces the ratio of the inter-droplet distance to the flame thickness.[6–9] Therefore, both water loading and droplet diameter play key roles in determining the ratio of inter-droplet distance to the flame thickness and evaporation Damköhler number. Furthermore, in addition to pertinent physical phenomena such as cooling and dilution, primarily evident in the temperature field, gaseous water can influence the flame structure, radical concentration, and flame propagation characteristics.[10,11] Nonetheless, given the low steam concentration considered in this analysis, the chemical effects of water injection remain weak for the present analysis and thus will not be addressed further in this paper. The investigation of flame topology, given its implications for modeling, has been extensively studied in the context of purely gaseous flames.[12–15] However, the effects of an interacting second phase and the water droplet diameter on the flame surface topology in spray flames where the fuel is supplied by liquid droplets are yet to be analyzed in detail.[16] This information is fundamentally important for the purpose of turbulent combustion modeling because the nature of flame topology is often quantified in terms of curvature statistics, which in turn affect the evolution of the flame surface density (FSD) and scalar dissipation rate (SDR) within the flame brush.[17,18] To address this gap in the existing literature, this paper focuses on the analysis of the effects of water injection on the flame surface topology and its implication on flame propagation statistics for both laminar and turbulent n-heptane spray flames for different initial mono-sized water droplet diameters based on carrier-phase three-dimensional direct numerical simulations (DNS). It is worth noting that the effects of fuel droplet diameter, overall equivalence ratio, and water loading on flame surface topology and local flame propagation characteristics have been addressed elsewhere[9,16,19–23] for different turbulence intensities for premixed and spray flames and thus are not considered here. Instead, the present analysis focuses on the effects of water droplet diameter and flow conditions (i.e., under laminar and moderate turbulence intensity conditions) on flame surface topology and local flame propagation. The flame surface topology is often characterized by flame curvature,[12] and thus, the curvature statistics will be the main focus of this paper. It is recognized that both tangential strain rate and curvature affect the local flame propagation characteristics, but it was demonstrated earlier by Rutland and Trouve[24] that the strain rate effects remain weak in the absence of significant differential diffusion effects and primarily impact the global flame characteristics. Thus, the effects of the tangential strain rate will not be addressed in this paper because the evaporation of droplets directly affects the flame curvature as a result of droplet-induced flame wrinkling, which in turn affects the flame topology. In this respect, the main objectives of the present analysis are: (a) to demonstrate the effects of water droplet injection on the topologies of reaction progress variable; (b) to explain the influence of water injection on local flame propagation for different initial mono-sized water droplet diameters and flow conditions.

The rest of the paper is organized as follows. The mathematical background and numerical implementation related to this analysis are provided in Secs. II and III. Following that the results will be presented and subsequently discussed in Sec. IV. Finally, the main findings will be summarized, and conclusions will be drawn in Sec. V.

II. MATHEMATICAL BACKGROUND

A modified single-step irreversible chemical reaction is employed in this work,[25] where the Zeldovich number β and the heat of combustion H are taken to be functions of equivalence ratio and used in the reaction rate defined through an Arrhenius-type expression:

$$\dot{\omega}_F = -\rho B^* Y_F Y_O \exp\left(\frac{-\beta(1-\theta)}{1-\alpha(1-\theta)}\right). \tag{1}$$

Here, the variable ρ denotes density, Y_F and Y_O denote the mass fractions of fuel and oxidizer, B^* is the pre-exponential factor, and α signifies the heat release parameter, derived from the adiabatic flame temperature under stoichiometric conditions and the unburnt gas temperature, given as $\alpha = (\hat{T}_{ad,(\phi_g=1)} - \hat{T}_0)/\hat{T}_{ad,(\phi_g=1)}$. In Eq. (1), θ represents the normalized temperature, defined as $\theta = (\hat{T} - \hat{T}_0)/(\hat{T}_{ad,(\phi_g=1)} - \hat{T}_0)$, where $\hat{T}$, $\hat{T}_0$, and $\hat{T}_{ad,(\phi_g=1)}$ represent the instantaneous dimensional temperature, unburned gas temperature, and adiabatic flame temperature of the stoichiometric mixture, respectively. The use of a single-step chemical model for the present study allows for a parametric analysis in terms of water droplet diameter and flow conditions without incurring an exorbitant computational cost. It was shown in previous studies[9,22] that the variation in laminar burning velocity $S_{b,(\phi_g)}$ with the gaseous equivalence ratio ϕ_g obtained from detailed chemistry simulations[26] can be captured with this chemical mechanism by choosing the appropriate value of B^*. It was also demonstrated elsewhere[9] that this chemical mechanism accurately predicts the influence of water loading in the unburnt gas on the laminar burning velocity obtained from a detailed chemical mechanism. Although simplification of chemistry is adopted here in favor of parametric analysis, it is also worth noting that either reduced/skeletal chemical mechanisms are used in most "detailed chemistry" DNS and these mechanisms are also not free from simplifications. The gaseous species are assumed to be perfect gases with unity Lewis number and have standard values of the ratio of specific heats ($\gamma = 1.4$) and the Prandtl number ($Pr = 0.70$). Statistically planar n-heptane-air spray flames with an overall equivalence ratio of $\phi_{ov} = \phi_g + \phi_l = 1.0$ (where ϕ_g is the equivalence ratio in the gaseous phase and ϕ_l is the equivalence ratio in the liquid phase), where the fuel is supplied in the form of liquid fuel droplets, are allowed to interact with different mono-sized spherical water droplets. The employment of mono-sized mists comprising fuel and water allows for the identification of the effects of droplet diameter in isolation. It is worth noting that the primary aim of the present study is to obtain fundamental physical insights rather than to simulate realistic technical applications, as is commonly expected in typical DNS endeavors. This approach is consistent with several previous DNS studies on droplet-laden combustion processes.[19–23,27–30] In this analysis, the liquid water and fuel droplets are individually tracked in a Lagrangian sense and their position, velocity, diameter, and temperature (i.e., $\vec{x}_d$, $\vec{u}_d$, a_d, T_d with the subscript d referring to droplet quantities) are obtained based on the following evolution relations:[9,16,19–23,29]

$$\frac{d\vec{x}_d}{dt} = \vec{u}_d; \quad \frac{d\vec{u}_d}{dt} = \frac{\vec{u}(\vec{x}_d,t) - \vec{u}_d}{\tau_d^u}; \quad \frac{da_d^2}{dt} = -\frac{a_d^2}{\tau_d^p};$$
$$\frac{dT_d}{dt} = \frac{\hat{T}(\vec{x}_d,t) - T_d - B_d L_v/C_P^g}{\tau_d^T}, \tag{2}$$

where $\vec{u}$ and $\hat{T}$ are gaseous-phase velocity vector and temperature, respectively; L_v is the latent heat of vaporization of liquid fuel or water,

as applicable. The relaxation timescales for droplet velocity τ_d^u, diameter τ_d^p and temperature τ_d^T in Eq. (2) are given by[9,16,19–23,27,29] $\tau_d^u = \rho_d a_d^2/(18C_u\mu)$; $\tau_d^p = (\rho_d a_d^2/4\mu)(Sc/Sh_c)/ln(1+B_d)$ and $\tau_d^T = (\rho_d a_d^2/6\mu)(Pr/Nu_c)[B_d/ln(1+B_d)]C_p^L/C_p^g$, respectively. Moreover, in Eq. (2), ρ_d is the droplet density, Sc stands for the Schmidt number ($Sc = Pr$ since $Le = 1$ in all the cases considered in this work), C_p^L denotes the specific heat for the liquid phase, $C_u = 1 + Re_d^{2/3}/6$ is the drag coefficient correction, Re_d is the droplet Reynolds number, B_d is the Spalding number, and Sh_c and Nu_c are the corrected Sherwood and Nusselt numbers, respectively, which are defined as follows:[9,16,19–23,27,29]

$$Re_d = \frac{\rho|\vec{u}(\vec{x}_d,t) - \vec{u}_d|a_d}{\mu}; \quad B_d = \frac{Y_\alpha^s - Y_\alpha^g(\vec{x}_d,t)}{1 - Y_\alpha^s};$$
$$Sh_c = Nu_c = 2 + \frac{0.555Re_d Sc}{(1.232 + Re_d Sc^{4/3})^{1/2}}. \quad (3)$$

Here, μ is the dynamic viscosity of the gaseous phase and C_p^g is the gaseous specific heat at constant pressure. In Eq. (3), Y_α^s is the vapor mass fraction of species α (where $\alpha = F, W$ for fuel and water, respectively) at the droplet surface. The partial pressure of the vapor at the droplet surface p_α^s is evaluated using the Clausius–Clapeyron relation as[9,16,19–23,27,29] $p_\alpha^s = p_{ref} \exp(L_v/R[(1/T_{ref}^s) - (1/T_d^s)])$ and $Y_\alpha^s = (1 + (W_g/W_\alpha) \times [p(\vec{x}_d,t)/p_\alpha^s - 1])^{-1}$, where T_{ref}^s represents the boiling point of species α (i.e., either fuel or water droplets, as applicable) at a reference pressure p_{ref} and T_d^s is taken to be T_d, with W_g and W_α being the molecular weights of the gaseous mixture and species α (i.e., either for fuel or water), respectively, and R is the universal gas constant. The drag model employed here is consistent with that proposed by Crowe et al.,[31] while the Sherwood number and the Nusselt number, which are considered identical in this study, are determined using the empirical formula introduced by Faeth and Fendell.[32] It is noteworthy to highlight that the equivalence observed between the Sherwood number and the Nusselt number, or between the Spalding number for heat transfer and mass transfer, is contingent upon the assumption of unity Lewis number within the droplet–gas interface. This assumption was invoked in several previous analyses.[19,27–30,33] Moreover, heavy hydrocarbons, such as n-heptane, degrade into lighter hydrocarbons such as methane upon heating, and these lighter hydrocarbons have Lewis numbers close to unity, and thus, a unity Lewis number assumption might hold without much loss of generality for the current analysis. The governing equations of mass, momentum, energy, and species conservation for the carrier phase can be given by the following generic partial differential equation:[9,16,19–23,27,29]

$$\frac{\partial(\rho\varphi)}{\partial t} + \frac{\partial(\rho u_j\varphi)}{\partial x_j} = \frac{\partial}{\partial x_j}\left[R_\varphi \frac{\partial\varphi_1}{\partial x_j}\right] + \dot{\omega}_\varphi + \dot{S}_{g\varphi} + \dot{S}_\varphi. \quad (4)$$

Here, $\varphi = \{1, u_i, e, Y_F, Y_O, Y_W\}$ and $\varphi_1 = \{1, u_i, \hat{T}, Y_F, Y_O, Y_W\}$ are used for the conservation equations of mass, momentum, energy, and mass fractions, respectively, $R_\varphi = \rho\nu/\sigma_\varphi$ for $\varphi = \{1, u_i, Y_F, Y_O, Y_W\}$, and $R_\varphi = \lambda$ for $\varphi = e$, respectively, where $e = \int_{\hat{T}_{ref}}^{\hat{T}} C_v d\hat{T} + u_i u_i/2$ is the specific stagnation internal energy with $\hat{T}_{ref}$ and C_v being the reference temperature and specific heat at constant volume, respectively. Here, ν, λ, and σ_φ are the kinematic viscosity, thermal conductivity, and an appropriate Schmidt number corresponding to φ, respectively.

On the right-hand side of Eq. (4), $\dot{\omega}_\varphi$ represents the reaction rate contribution, $\dot{S}_{g\phi}$ is the appropriate source term in the gaseous-phase conservation equation, and $\dot{S}_\varphi = -(1/V_{cell})\sum d(m_d\varphi_d)/dt$ is the term arising from droplet evaporation, which is responsible for two-way coupling with $m_d = \rho_d(1/6)\pi a_d^3$ being the droplet mass.

A reaction progress variable c, which increases monotonically from 0.0 in the unburnt gas to 1.0 in the fully burnt gas, can be defined based on oxygen mass fraction, Y_O and mixture fraction $\xi = (Y_F - Y_O/s + Y_{O\infty}/s)/(Y_{F\infty} + Y_{O\infty}/s)$ in the following manner:[9,16,19–23,27,29]

$$c = \frac{Y_{O,u}(\xi) - Y_O}{Y_{O,u}(\xi) - Y_{O,b}(\xi)}. \quad (5)$$

Here, $Y_{O\infty} = 0.233$ is the oxygen mass fraction in air and $Y_{F\infty} = 1.0$ is the fuel mass fraction in the pure fuel stream, and $Y_{Ou}(\xi) = Y_{O\infty}(1-\xi)$ and $Y_{Ob}(\xi) = max(0, (\xi - \xi_{st})/\xi_{st})Y_O^\infty$ are equilibrium mass fractions of oxygen in the unburnt gas and burnt gas mixture, respectively. For n-heptane, C_7H_{16}, $s = 3.52$ is the stoichiometric mass ratio of oxidizer to fuel and $Y_{Fst} = 0.0621$ and $\xi_{st} = 0.0621$ are the corresponding stoichiometric fuel mass fraction and mixture fraction, respectively.

The transport equation of the reaction progress variable, c, is given as[9,16,19–23]

$$\rho\left[\frac{\partial c}{\partial t} + u_j\frac{\partial c}{\partial x_j}\right] = \frac{\partial}{\partial x_j}\left[\rho D\frac{\partial c}{\partial x_j}\right] + \dot{w}_c + \dot{S}_{liq,c} + \dot{A}_c. \quad (6)$$

In Eq. (6), D is the molecular diffusivity of the reaction progress variable, $\dot{w}_c$ indicates the reaction rate of the reaction progress variable, $\dot{S}_{liq,c}$ represents the source/sink term arising due to droplet evaporation, and $\dot{A}_c$ is the cross-scalar dissipation term arising due to mixture inhomogeneity, which are expressed in the following manner using Burke–Schumann relations for $Y_{Ou}(\xi)$ and $Y_{Ob}(\xi)$:[9,16,19–23,27,29]

$$\dot{w}_c = \begin{cases} -\dfrac{\xi_{st}\dot{w}_O}{Y_{O\infty}\xi(1-\xi_{st})} & \text{if} \quad \xi \leq \xi_{st}, \\[3mm] -\dfrac{\dot{w}_O}{Y_{O\infty}(1-\xi)} & \text{if} \quad \xi > \xi_{st}, \end{cases} \quad (7a)$$

$$\dot{S}_{liq,c} = \begin{cases} -\dfrac{\xi_{st}}{Y_{O\infty}\xi^2(1-\xi_{st})}\left[\xi\dot{S}_O + (Y_{O\infty} - Y_O)\dot{S}_\xi\right] & \text{if} \quad \xi \leq \xi_{st}, \\[3mm] -\dfrac{1}{Y_{O\infty}(1-\xi)^2}\left[(1-\xi)\dot{S}_O + Y_O\dot{S}_\xi\right] & \text{if} \quad \xi > \xi_{st}, \end{cases} \quad (7b)$$

$$\dot{A}_c = \begin{cases} 2\rho D\nabla\xi \cdot \dfrac{\nabla c}{\xi} & \text{if} \quad \xi \leq \xi_{st}, \\[3mm] -2\rho D\nabla\xi \cdot \dfrac{\nabla c}{(1-\xi)} & \text{if} \quad \xi > \xi_{st}. \end{cases} \quad (7c)$$

In Eq. (7), $\dot{w}_O$ is the reaction rate of the oxidizer, $\dot{S}_\xi = (\dot{S}_F - \dot{S}_O/s)/(Y_{F\infty} + Y_{O\infty}/s)$ is the droplet source/sink term in the mixture fraction transport equation, $\dot{S}_F = \Gamma_F - \Gamma_m Y_F$ and $\dot{S}_O = -\Gamma_m Y_O$ are the droplet source/sink terms in the mass fraction transport equations for fuel and oxygen, respectively, Γ_m is the source term in the mass conservation equation due to the evaporation of liquid fuel and water, and Γ_F is the evaporation rate of fuel droplets.

Equation (6), for a given c isosurface, reads:[19,21–23] $\partial c/\partial t + u_j \partial c/\partial x_j = S_d |\nabla c|$, where S_d is the displacement speed, which is given as[19,21–23]

$$S_d = \frac{\left[\nabla \cdot (\rho D \nabla c) + \dot{w}_c + \dot{S}_{liq,c} + \dot{A}_c \right]}{\rho |\nabla c|} = S_n + S_t + S_r + S_s + S_z. \tag{8}$$

In Eq. (8), $S_n = \vec{N} \cdot \nabla(\rho D \vec{N} \cdot \nabla c)/\rho |\nabla c|$, $S_t = -2D\kappa_m$, and $S_r = \dot{w}_c/\rho |\nabla c|$ represent the normal diffusion, tangential diffusion, and reaction components (where $\vec{N} = -\nabla c/|\nabla c|$ is the local flame normal vector and $\kappa_m = 0.5\nabla \cdot \vec{N}$ is the flame curvature), and $S_z = \dot{A}_c/\rho |\nabla c|$ and $S_s = \dot{S}_{liq,c}/\rho |\nabla c|$ are the contributions arising from cross-scalar dissipation term and droplet evaporation, respectively. It can be appreciated from Eq. (8) that density ρ variation can affect the displacement speed S_d and its components (i.e., S_n, S_t, S_r, S_z, and S_s). Thus, the density-weighted displacement speed $S_d^* = \rho S_d/\rho_0$ and its components: $S_r^* = \rho S_r/\rho_0$, $S_n^* = \rho S_n/\rho_0$, $S_t^* = \rho S_t/\rho_0$, $S_z^* = \rho S_z/\rho_0$, and $S_s^* = \rho S_s/\rho_0$ (where ρ_0 is the unburnt gas density) are considered here because S_d^* statistics are necessary for the FSD,[17] SDR,[18] and level set[34]-based modeling methodologies. The principles underlying the characterization of S_d and the progress variable c originate from the theoretical framework of premixed flame propagation, whereas partially premixed combustion occurs in spray flames. Nevertheless, findings from a prior study,[16] utilizing an identical dataset of simulations, illustrate that the combustion predominantly occurs in premixed mode, justifying the use of these quantities in the present analysis. It is also worth noting that reaction progress variable and displacement speed were extensively used for partially premixed flames including spray combustion by several other authors.[30,35–38] In the present analysis, the reaction progress variable represents the normalized oxidizer mass fraction, which is consistent with previous attempts of spray combustion modeling analysis using the flamelet generated manifold[39] and the chemistry is often parameterized using c and ξ in the tabulated chemistry approach, especially in the context of partially premixed combustion.[40–42] Thus, displacement speed and topology of c isosurfaces are important from the point of view of modeling. This further justifies the use of displacement speed of c isosurface instead of the displacement speed of the Y_F isosurface for the current analysis.

It can be appreciated from the definitions of S_t and S_t^* that the flame curvature κ_m plays a key role in local flame propagation statistics. The flame curvature $\kappa_m = 0.5\nabla \cdot \vec{N}$ can be expressed as[12]

$$\kappa_m = 0.5(\kappa_1 + \kappa_2) = -0.5 I_1, \tag{9}$$

where κ_1 and κ_2 are the principal curvatures of the flame surface and eigenvalues of the curvature tensor with components given by $\partial N_i/\partial x_j$ and I_1 is the first invariant of the curvature tensor. The second invariant I_2 of the curvature tensor is given by[12]

$$I_2 = \kappa_1 \kappa_2 = \kappa_g. \tag{10}$$

The second invariant I_2 is alternatively known as the Gauss curvature. The third invariant $I_3 = det(\partial N_i/\partial x_j)$ is identically zero for the curvature tensor. Therefore, the flame surface topology can be characterized in terms of κ_m and κ_g. The phase space, given by $\kappa_m^2 > \kappa_g$, is physically unrealizable because κ_1 and κ_2 become complex numbers under this condition. The realizable condition given by $\kappa_m > 0$ and $\kappa_g > 0$ is

representative of cup convex flame surface topology, whereas the condition given by $\kappa_m < 0$ and $\kappa_g > 0$ is representative of cup concave flame surface topology.[12] By contrast, $\kappa_m > 0$ and $\kappa_g < 0$ is representative of convex saddle-type flame surface topology, whereas $\kappa_m < 0$ and $\kappa_g < 0$ represent a concave saddle topology.[12] Moreover, the realizable region, given by $\kappa_m > 0$ and $\kappa_g = 0$, is representative of a convex cylindrical flame surface topology, whereas $\kappa_m < 0$ and $\kappa_g = 0$ is representative of a concave cylindrical flame surface topology.[12] The condition, given by $\kappa_m = 0$ and $\kappa_g = 0$, represents a flat flame surface. The influence of droplet-induced wrinkling of the c isosurfaces and their implications on the local flame propagation characteristics are discussed in Sec. IV.

III. NUMERICAL IMPLEMENTATION

All the simulations conducted in this paper are carried out using a well-known DNS code SENGA+,[9,16,19–23,27,29] where the conservation equations of mass, momentum, energy, and species are solved in non-dimensional form. In SENGA+, high-order finite-difference (10th order central difference for the internal grid points with a gradual decrease on the order of accuracy to a second-order one-sided scheme at the non-periodic boundaries) and Runge–Kutta (third-order low-storage) schemes are used for spatial discretization and time advancement, respectively. For this analysis, DNS of statistically planar spray n-heptane–air flames with $\phi_{ov} = 1.0$ have been carried out under laminar conditions and for an initial value of the normalized root mean square turbulent velocity of $u'/S_{b,(\phi_g=1)} = 4.0$ with a non-dimensional longitudinal integral length scale of $L_{11}/\delta_{st} = 2.5$, where $\delta_{st} = (\hat{T}_{ad,(\phi_g=1)} - \hat{T}_0)/max|\nabla \hat{T}|_L$ is the thermal flame thickness of the stoichiometric mixture. These values of $u'/S_{b,(\phi_g=1)}$ and L_{11}/δ_{st} yield a Damköhler number of $Da = L_{11}S_{b,(\phi_g=1)}/\delta_{st}u' = 0.625$, and a Karlovitz number of $Ka = (u'/S_{b,(\phi_g=1)})^{1.5}(L_{11}/\delta_{st})^{-0.5} = 5.0$, which are representative of the thin reaction zone regime combustion.[34] It is important to note that a moderate turbulence intensity is considered for the current analysis because the droplet-induced effects on flame topology and flame propagation are eclipsed by turbulence-induced flame wrinkling for large values of $u'/S_{b,(\phi_g=1)}$, as indicated by several previous analyses.[19,20,43,44] For the present analysis, the thermodynamic pressure is taken to be atmospheric and the unburnt gas temperature is considered to be 300 K, which yields a heat release parameter $\tau = (\hat{T}_{ad,(\phi_g=1)} - \hat{T}_0)/\hat{T}_0$ of 6.54. Additional cases representative of spray n-heptane-air flames without any water loading are also considered for the sake of comparison with the corresponding cases with water injection. The simulation domain for the present analysis is considered to be $30\delta_{st} \times 20\delta_{st} \times 20\delta_{st}$, and a uniform Cartesian grid of $384 \times 256 \times 256$ is used to discretize this domain. This grid remains smaller than the Kolmogorov length scale η and accommodates 10 grid points within δ_{st} (and more than 2-grid points for η, since $\eta/\delta_{st} = 0.32$). For these simulations, the direction of the mean flame propagation is taken to align with the long side of the simulation domain (i.e., x direction in this configuration). The boundaries in x direction are taken to be partially non-reflecting and are specified using the Navier–Stokes characteristic boundary condition technique.[45] The transverse domain boundaries are taken to be periodic. For the present analysis, two different initial mono-sized water droplets (i.e., $a_d/\delta_{st} = 0.02$ and 0.04, which corresponds to a range of 10–20μm) have been considered for a water

TABLE I. Thermo-physical properties of liquid n-heptane and water.

	n-heptane	Water	Unit
Density	684	999.9	kg/m^3
Molecular mass	100.0	18.2	g/mol
Latent heat of vaporization (at boiling temperature)	315.0	2258.0	kJ/kg
Specific heat at constant pressure	2296.45	4181.0	J/kg/K
Boiling temperature	371	373	K

loading of $Y_W^{ov} = m_W/(m_W + m_A) = 0.1$, where Y_W^{ov} is the mass fraction of water (in both liquid (l)+ gaseous (g) phases) in the unburnt gas (and thus independent of the chemical reaction) with m_W being the total amount of water injected in a mass of air given by m_A. The fuel droplets are considered to have an initial normalized diameter of $a_d/\delta_{st} = 0.04$ for this analysis, and the effects of fuel droplet diameter have been addressed elsewhere[9,16,19–22] and thus are not discussed here. For the simulations considered here, both fuel and water droplets are introduced with a constant initial diameter. The initial diameter distribution of the fuel droplets results from the preceding evolution of the monodisperse mist, aimed at achieving a stable flame before interacting with the water droplets. The fuel and water droplets are randomly placed in a statistically homogeneous manner within the unburnt gas part of the domain as a part of the initialization. The thermo-physical properties of the two liquids are reported in Table I. The huge difference in the latent heat of evaporation and other properties such as specific heat and density is visible from Table I. The Stokes number for both water and fuel droplets can be defined based on the turbulent timescale (i.e., L_{11}/u') as $St = \tau_p L_{11}/u' = \rho_d a_d^2 u'/(18 C_u \mu L_{11})$, and it remains smaller than 0.06 for the largest droplets in the turbulent cases with $u'/S_{b,(\phi_g=1)} = 4.0$. Alternatively, the maximum Stokes number $St' = \tau_p S_{b,(\phi_g=1)}^2/\alpha_{T0} = \rho_d a_d^2 S_{b,(\phi_g=1)}^2/(18 C_u \mu \alpha_{T0})$ based on the chemical timescale (i.e., $\alpha_{T0}/S_{b,(\phi_g=1)}^2$, where α_{T0} is the thermal diffusivity) remains smaller than 0.20 for the largest droplets considered in this analysis. The droplet volume fraction remains much smaller than 0.01% for the cases considered here. The ratio a_d/η is 0.06, 0.12 for $a_d/\delta_{st} = 0.02$ and 0.04, respectively, for $u'/S_{b,(\phi_g=1)} = 4.0$ and the mean normalized inter-droplet distance s_d/η ranges between 2.48 and 4.35. For $a_d/\delta_{st} = 0.02$ and 0.04, the ratio of the initial droplet volume to the computational cell volume V_d/V_{cell} is 0.007 and 0.057, respectively, which justifies the point source assumption and is comparable to several previous analyses.[9,16,19–22,27–30,33,46]

A standard pseudo-spectral method is used to generate initial divergence-free, homogeneous isotropic turbulent velocity fluctuations following Batchelor–Townsend spectrum,[47] which is also injected at the inflow to maintain the turbulence intensity. At the same time, the scalar field is initialized by a steady-state unstrained spray flame solution generated using the commercial software package COSILAB,[48] as done in several previous analyses.[19–22,49] The flame–turbulence interaction takes place under spatially decaying turbulence and statistics are taken at $4t_{chem} = 4\alpha_{T0}/S_{b,(\phi_g=1)}^2$, which amounts to $4.35 L_{11}/u'$ for initial $u'/S_{b,(\phi_g=1)} = 4.0$. This simulation time is consistent with several previous analyses,[9,16,27,29,30,33] and both the volume-integrated burning rate and flame surface area reached a quasi-stationary state by the end of the simulation.[16,23] This can be substantiated by the temporal

evolutions of the volume-integrated burning rate and flame surface area for the cases considered here, which were presented elsewhere[16] and thus are not repeated here. In Sec. IV of this paper, statistical analyses are conducted across various intervals of the progress variable. Sampling is performed within the entire flame when the progress variable falls within the range of $0.1 \leq c \leq 0.9$. Conversely, when examining statistics within the pre-heating region, the range is restricted to $0.4 \leq c \leq 0.6$, while within the reaction-dominated region, the interval is defined as $0.7 \leq c \leq 0.95$. Subsequently, for the probability density function (PDF) of the burnt gas side temperature, values of c greater than 0.7 are exclusively considered. This selection aims to focus solely on regions strongly influenced by water evaporation and in which the reaction term is dominant, thereby excluding phenomena occurring within the unburnt region of the flame. The assertions made earlier regarding the reaction-dominated region for the present thermochemistry of n-heptane–air mixtures can be substantiated by the results shown in several previous analyses,[19,50,51] which include the profiles of various terms in the transport equation of the progress variable conditioned upon c. This information is not repeated here and interested readers are referred to Refs. 19, 50, and 51 for further information in this regard.

IV. RESULTS AND DISCUSSION
A. Droplet effects on flame morphology

The instantaneous views, from the product side, of the isosurfaces of $c = 0.75$ and $\theta = 0.75$ are shown in Fig. 1, respectively, for the water injection case with an initial water droplet diameter of $a_d/\delta_{st} = 0.04$ for both laminar and turbulent flow conditions. For unstretched laminar premixed n-heptane–air flames, the maximum heat release rate occurs at $c \approx 0.75$ and $\theta \approx 0.75$ for the current thermochemistry,[9,21] and thus, these isosurfaces have been chosen as the visual representation of the flame in Fig. 1. It can be seen from Fig. 1 that c and θ isosurfaces are not identical to each other for these flames. The latent heat extraction of the water droplets gives rise to dimples on the $\theta = 0.75$ isosurface, whereas water droplets do not impart any significant distortion to the $c = 0.75$ isosurface. This is particularly visible in the laminar case. It is worth noting that the evaporation of water droplets can potentially dilute the concentration of reactants, but this effect is relatively weak, which was demonstrated elsewhere.[9,16] The weak dilution effect of the water vapor is a result of the relatively low volatility of water in comparison with fuel droplets (see Table I). As a result, the fuel droplets rarely reach the hot gas side of the flame and the gaseous fuel has more time for mixing, whereas the water droplets penetrate far into the post-flame region (i.e., $c = 1.0$). In order to explain the observations made from Fig. 1, the distributions of non-dimensional temperature θ and mass fraction of evaporated water (i.e., it does not include the water vapor produced by chemical reaction) Y_W^g in the central midplane for the turbulent case with an initial normalized droplet diameter of $a_d/\delta_{st} = 0.04$ for both water and fuel droplets and an initial turbulence intensity of $u'/S_{b,(\phi_g=1)} = 4.0$ are shown in Fig. 2. The contours of $c = 0.1$, 0.5, and 0.9 (from left to right) are superimposed on non-dimensional temperature θ and mass fraction of evaporated water Y_W^g fields in Fig. 2.

Moreover, it can be appreciated from Fig. 1 that the physical locations of $c = 0.75$ and $\theta = 0.75$ are different from each other. It can be seen from Fig. 2 (left) that the non-dimensional temperature θ remains significantly different from c within the flame front and θ assumes a
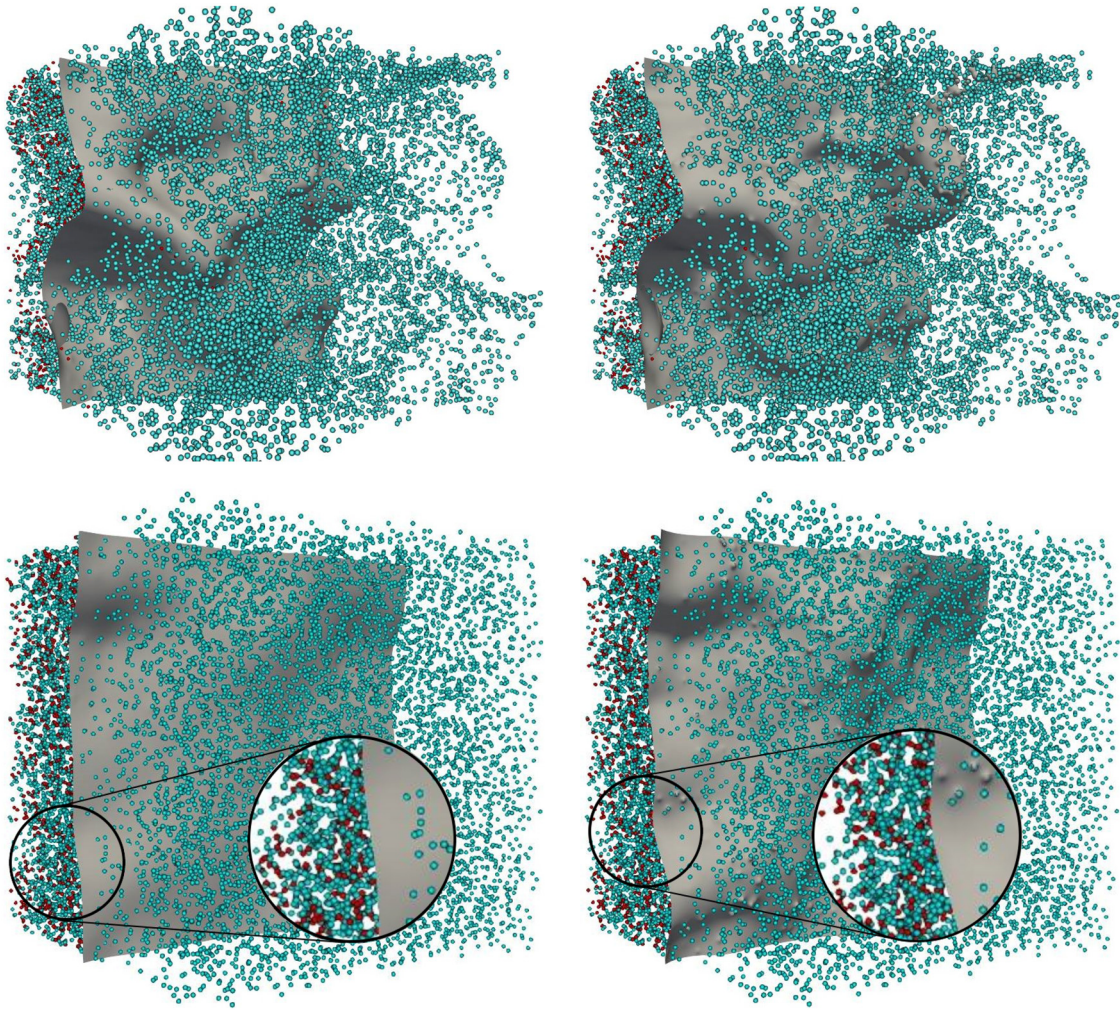
FIG. 1. Isosurfaces of reaction progress variable $c = 0.75$ (left) and non-dimensional temperature $\theta = 0.75$ (right) at $t = 4.0t_{chem}$ for the turbulent spray flame case with water addition with initial $u'/S_{b,(\phi_g=1)} = 4.0$ (top) and laminar conditions (bottom). Not-to-the-scale spheres indicate the fuel droplets (red) and water droplets (blue). The point of view is in the product side.
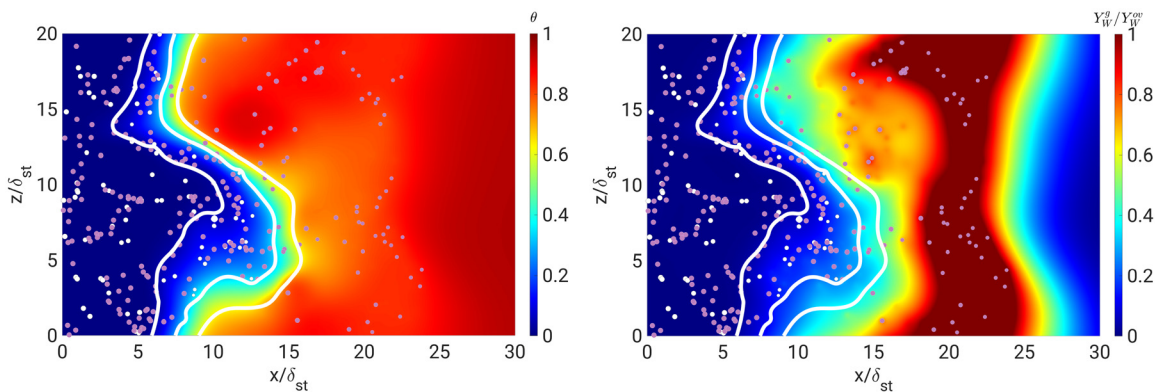
FIG. 2. Midplane contours of non-dimensional temperature θ (left) and steam mass fraction Y_W^g excluding the product water (right) at $t = 4.0t_{chem}$. Not-to-the-scale dots indicate the fuel droplets (white) and water droplets (pink), both of the initial size of $a_d/\delta_{st} = 0.04$. White isolines represent $c = 0.1, 0.5, 0.9$ (left to right), respectively.

value significantly smaller than 1.0 (which is indicative of the adiabatic flame temperature for $\phi_g = 1.0$). This is a consequence of a predominantly fuel–lean inhomogeneous mixture in the gaseous phase (i.e., $\phi_g < 1.0$) due to incomplete evaporation of fuel droplets because of their finite evaporation time, which can be substantiated by the probability density functions (PDFs) of ϕ_g within the flame front characterized by $0.1 \leq c \leq 0.9$ shown in Fig. 3, on the left, for all cases considered here. It can be seen from Fig. 3 (left) that the PDFs of ϕ_g peak at $\phi_g < 1.0$ for all cases and the PDFs of $\phi_g = \xi(1 - \xi_{st})/[\xi_{st}(1 - \xi)]$ are wider with a higher probability of finding $\phi_g < 1.0$ mixture for the turbulent cases as a result of the combined effects of turbulent dispersion and mixing of the evaporated fuel vapor. The predominance of fuel–lean burning, despite having $\phi_{ov} = 1.0$ in spray flames, is consistent with the findings of several previous analyses on turbulent spray flames.[19–22]

It can further be seen from Fig. 2 (right) that Y_W^g remains considerably smaller than Y_W^{ov} within the flame front, which is indicative of the fact that the evaporation of water droplets does not significantly dilute the reacting mixture. Figure 2 (right) further suggests that the evaporation of water droplets principally takes place in the post-flame region within the burnt gas, as shown in previous analyses.[9,16,23] Thus, the extraction of latent heat of evaporation by the water droplets acts to reduce the temperature of the burnt gas, which can be seen from the reduction in the probability of finding high values of θ in the case of water injection in Fig. 3 (right) where the PDFs of θ for the region corresponding to $c > 0.70$ are shown for the cases considered here. The cooling effects due to water droplet evaporation are particularly prevalent for smaller water droplets owing to their faster evaporation rates. The PDFs of θ for the region corresponding to $c > 0.70$ are wider in the turbulent cases than in the laminar cases because of enhanced mixing due to turbulent motion. Furthermore, the bi-modal temperature distribution depicted in Fig. 3 (right) indicates the presence of unburnt fuel within the flame. Typically, this unburnt fuel is situated within the evaporation clouds of n-heptane droplets, which undergoes combustion

in the hotter regions of the flame, after mixing with the surrounding air, leading to a subsequent increase in temperature.

It can further be seen from Fig. 3 (left) that the probability of finding fuel–lean mixture is found to be smaller in the water injection case with small initial water droplet diameter (e.g., $a_d/\delta_{st} = 0.02$) than in the cases without water injection and large water droplet diameter (e.g., $a_d/\delta_{st} = 0.04$) for both laminar and turbulent cases. The cooling effect induced by small water droplets acts to weaken the effects of thermal expansion and flame normal acceleration. This was demonstrated by the present authors elsewhere[16] and can also be verified from the PDFs of normalized dilatation rate $\nabla \cdot \mathbf{u} \times \delta_{st}/S_{b,(\phi_g=1)}$ for turbulent (left) and laminar (right) cases in Fig. 4, which indicates that the strength of flame normal acceleration due to thermal expansion weakens with decreasing a_d/δ_{st}. This effect gives rise to an increase in the residence time of the fuel droplets within the flame front and thereby fuel droplets get more time to fully evaporate and the resulting fuel vapor gets more time to mix with the surrounding gaseous mixture with the weakening of the flame normal acceleration for small water droplets.

It can be appreciated from the foregoing discussion that water injection is likely to have a significant influence on the flame surface topology and its propagation characteristics, which will be discussed next in this paper.

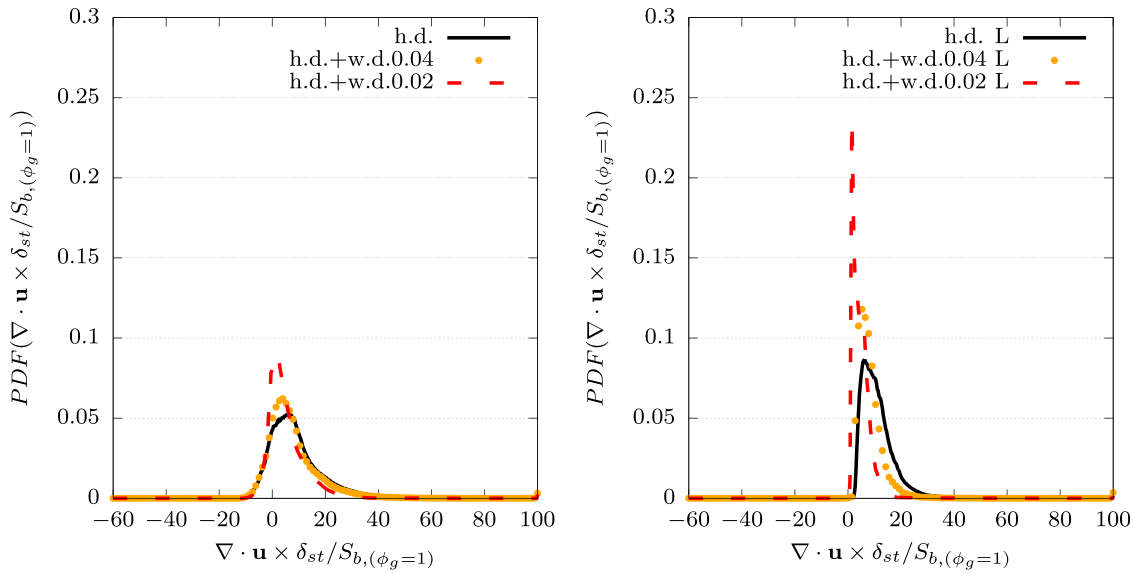## B. Distribution of flame surface topologies

The contours of joint PDFs between $\kappa_m \times \delta_{st}$ and $\kappa_g \times \delta_{st}^2$ for the reaction progress variable isosurfaces in the regions given by $0.4 \leq c \leq 0.6$ (representative of the preheat zone) and $0.7 \leq c \leq 0.95$ (representative of the reaction zone) for all turbulent cases considered here are shown in Fig. 5. The corresponding joint PDFs between $\kappa_m \times \delta_{st}$ and $\kappa_g \times \delta_{st}^2$ for the corresponding laminar cases are shown in Fig. 6. The most probable value of κ_m remains close to zero for all cases, as expected for statistically planar flames considered here.
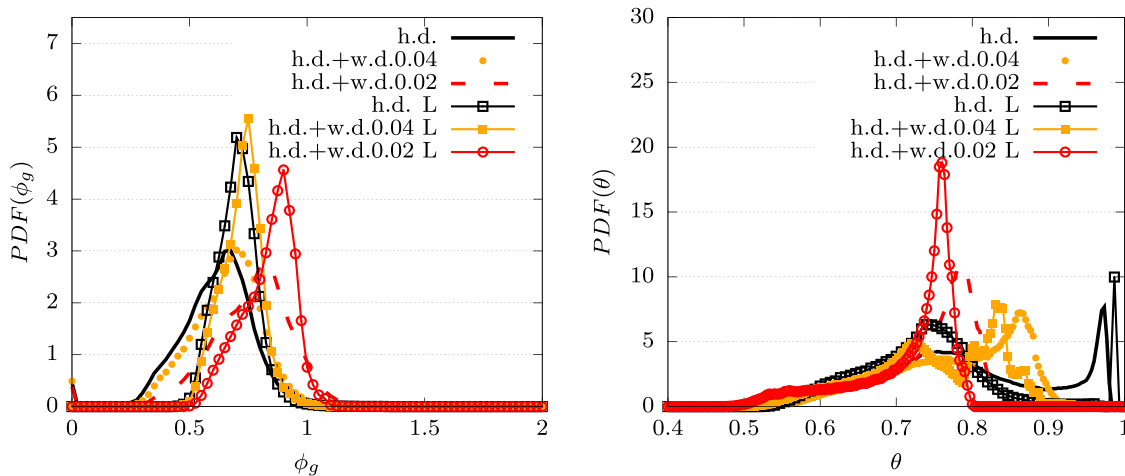

FIG. 3. PDFs of ϕ_g within the flame front characterized by $0.1 \leq c \leq 0.9$ (left) and θ for the region corresponding to $c > 0.70$ (right) for laminar (line with symbols) and turbulent condition with initial $u'/S_{b,(\phi_g=1)} = 4.0$ (continuous line or markers). In the legend, h. stands for heptane, d. stands for droplets, and w. stands for water. The number refers to the initial water diameter, and L stands for laminar. The same nomenclature is used also in the following figures. The markers in Fig. 3 and subsequent figures provide an idea of the number of bins employed for the generation of these PDFs. The bin number is chosen such that it shows the distribution for the whole range of samples without excessive numerical noise.

FIG. 4. PDFs of dilatation rate $\nabla \cdot \mathbf{u} \times \delta_{st}/S_{b,(\phi_g=1)}$ in the domain portion with $0.1 \leq c \leq 0.9$ for initial turbulence intensity of $u'/S_{b,(\phi_g=1)} = 4.0$ (left) and laminar (right). The statistics are taken at $t = 4.0 t_{chem}$.
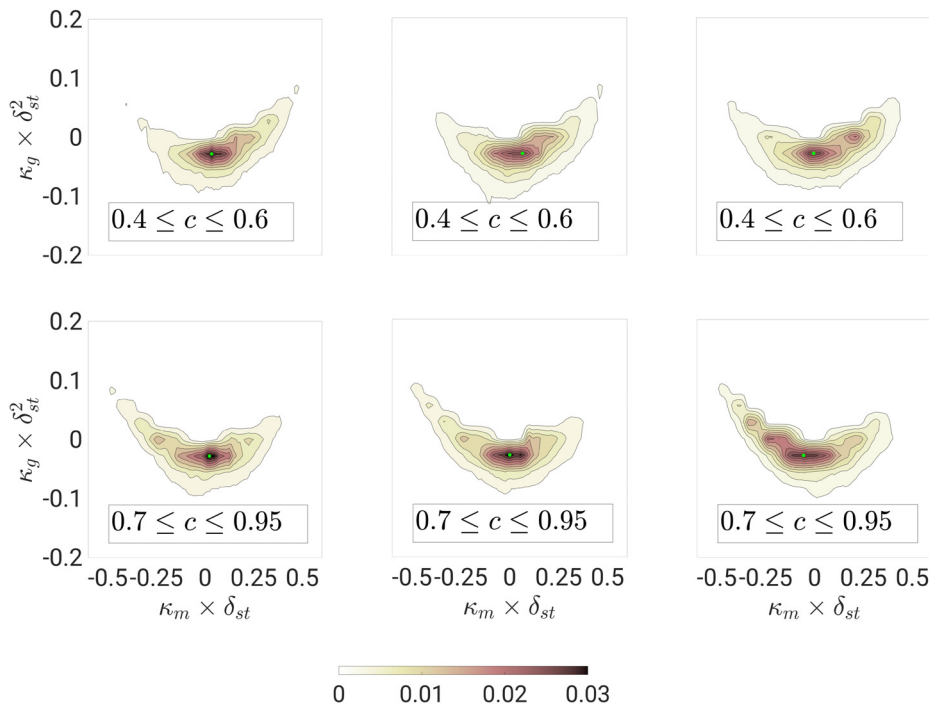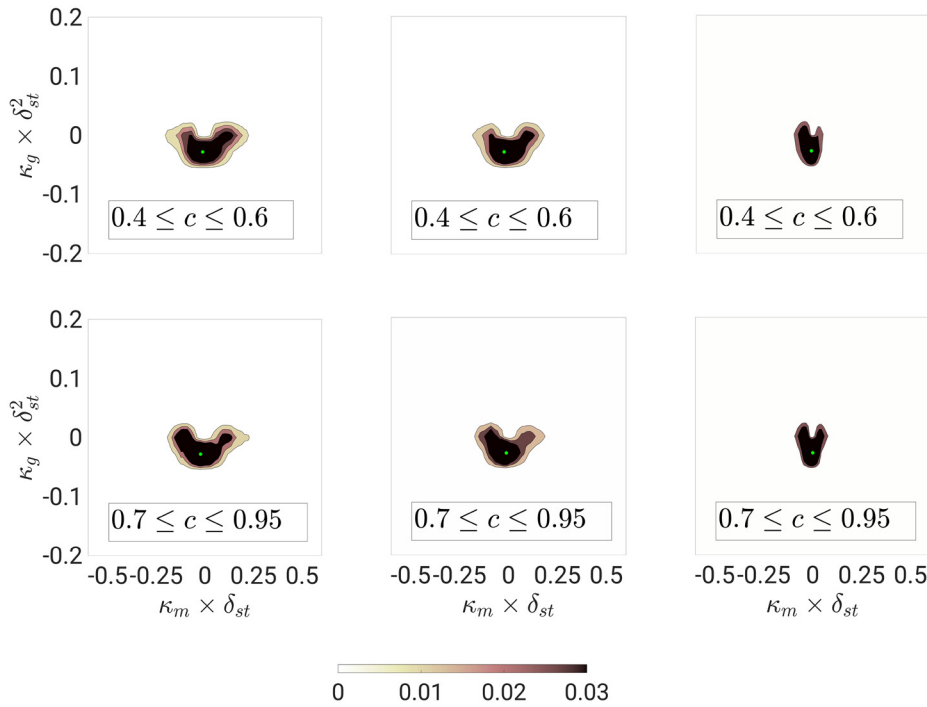

FIG. 5. Joint PDFs between $\kappa_m \times \delta_{st}$ and $\kappa_g \times \delta_{st}^2$ for the reaction progress variable isosurfaces in the regions given by $0.4 \leq c \leq 0.6$ (top row) and $0.7 \leq c \leq 0.95$ (bottom row) for the cases without droplets (left), and for cases with an initial water droplet size of $a_d/\delta_{st} = 0.04$ (middle) and 0.02 (right) for the turbulent condition with initial $u'/S_{b,(\phi_g=1)} = 4.0$.

The spread of the joint PDFs is comparable for the turbulent cases with and without water injection, but water injection gives rise to narrowing of the range of $\kappa_m \times \delta_{st}$ for the laminar cases and this effect is particularly strong for water droplets with small diameters.

The effects of water injection become more prominent for smaller water droplets due to faster evaporation (cf. diameter squared law).

The non-zero values of κ_m for the laminar case without water injection are indicative of fuel droplet-induced flame wrinkling. The fuel droplet-induced deformations of c isosurfaces are weakened by the cooling effect induced by the latent heat of evaporation of water droplets. The dampening of flame wrinkling as a result of water injection with small water droplet diameter is eclipsed by turbulence-induced

FIG. 6. Joint PDFs between $\kappa_m \times \delta_{st}$ and $\kappa_g \times \delta_{st}^2$ for the reaction progress variable isosurfaces in the regions given by $0.4 \leq c \leq 0.6$ (top row) and $0.7 \leq c \leq 0.95$ (bottom row) for the cases without droplets (left), and for cases with an initial water droplet size of $a_d/\delta_{st} = 0.04$ (middle) and 0.02 (right) for the laminar condition.

flame wrinkling, and thus, the joint PDFs between $\kappa_m \times \delta_{st}$ and $\kappa_g \times \delta_{st}^2$ both in the preheat and reaction zones for cases with and without water injection are found to be comparable (see Fig. 5), whereas a significant difference in behavior is observed for the laminar cases as a result of water injection, especially for small water droplet diameters. In order to explain this behavior, it is instructive to consider the effects of water injection on flame propagation characteristics and its interrelation with flame surface topology.

For the sake of completeness, it is worth mentioning that the correlation between c and ϕ_g has been found to be weak and their joint PDF seems to indicate statistical independence between these quantities for all the cases considered here (not shown here to avoid digression). Thus, the joint PDF of c and ξ in the flamelet-based closures[41,42] can be approximated by the product of marginal PDFs of these quantities for the flames considered here.

C. Interrelation between isosurface topology and flame propagation

The cooling effects induced by water droplet evaporation can further be substantiated by Fig. 7 (top-left) where the variations of the normalized mean value of the density-weighted displacement speed $S_d^*/S_{b,(\phi_g=1)} = S_d \rho / \rho_0 S_{b,(\phi_g=1)}$ within the region given by $0.1 \leq c \leq 0.9$, shows a monotonic drop in the mean value of S_d^* with decreasing water droplet diameter for both laminar and turbulent flow conditions. This is a consequence of the strengthening of the cooling effect associated with evaporation with a decrease in water droplet diameter. This acts to reduce the magnitude of $\dot{w}_c$ within the reaction zone in the case of water injection especially for small water droplets (e.g., water droplets with initial $a_d/\delta_{st} = 0.02$), which leads to a decrease on the mean value of S_d^*. The contributions of $(S_s^* + S_z^*)$ remain negligible

in comparison to S_r^*, S_n^*, and S_t^* (not shown for the sake of brevity), which is consistent with previous analyses.[19,21,23] The weakening of the chemical reaction effects is also reflected in the reduction of the normalized burning velocity $S_F/S_{b,(\phi_g=1)}$ (where $S_F = 1/(\rho_0 A_0) \int_V \dot{w}_c dV$ with A_0 being the projected flame area in the direction of mean flame propagation, which is the cross-sectional area of the simulation domain, in this configuration, and V is the flame volume) as a result of water injection in Fig. 7 (top-right), which shows that the extent of this reduction increases with decreasing water droplet diameter. The temporal evolution of the burning velocity is documented in a previous study by the same authors,[16] where this quantity was analyzed for cases involving spray combustion and premixed combustion with water injection.

It can further be seen from Fig. 7 (top-left) that the mean values of S_d^* in turbulent cases are smaller than the corresponding laminar flame cases. It has been demonstrated earlier in Fig. 3 (left) that the probability of finding a fuel–lean mixture (i.e., $\phi_g < 1$) is higher in turbulent cases than in the corresponding laminar cases, which acts to reduce the magnitude of S_r^*. This trend alongside turbulent stretching yields a reduced magnitude of the mean value of S_d^* for turbulent cases in comparison to the corresponding laminar cases irrespective of the water droplet diameter.

In addition to the mean value, the local flame topology dependence of S_d^* is also affected by water injection. The correlation coefficients between S_d^* and κ_m and between S_d^{*2} and κ_g in the cases considered here are shown for the reaction zone given by $0.1 \leq c \leq 0.9$ in Figs. 7 (bottom-left) and (bottom-right), respectively. It can be seen from Fig. 7 (bottom-left) that S_d^* is negatively correlated with κ_m for all cases but the correlation strengths for the cases without water droplets and with large water droplets are found to be stronger than that obtained for the corresponding water injection cases with small initial water droplet diameter under both laminar and turbulent
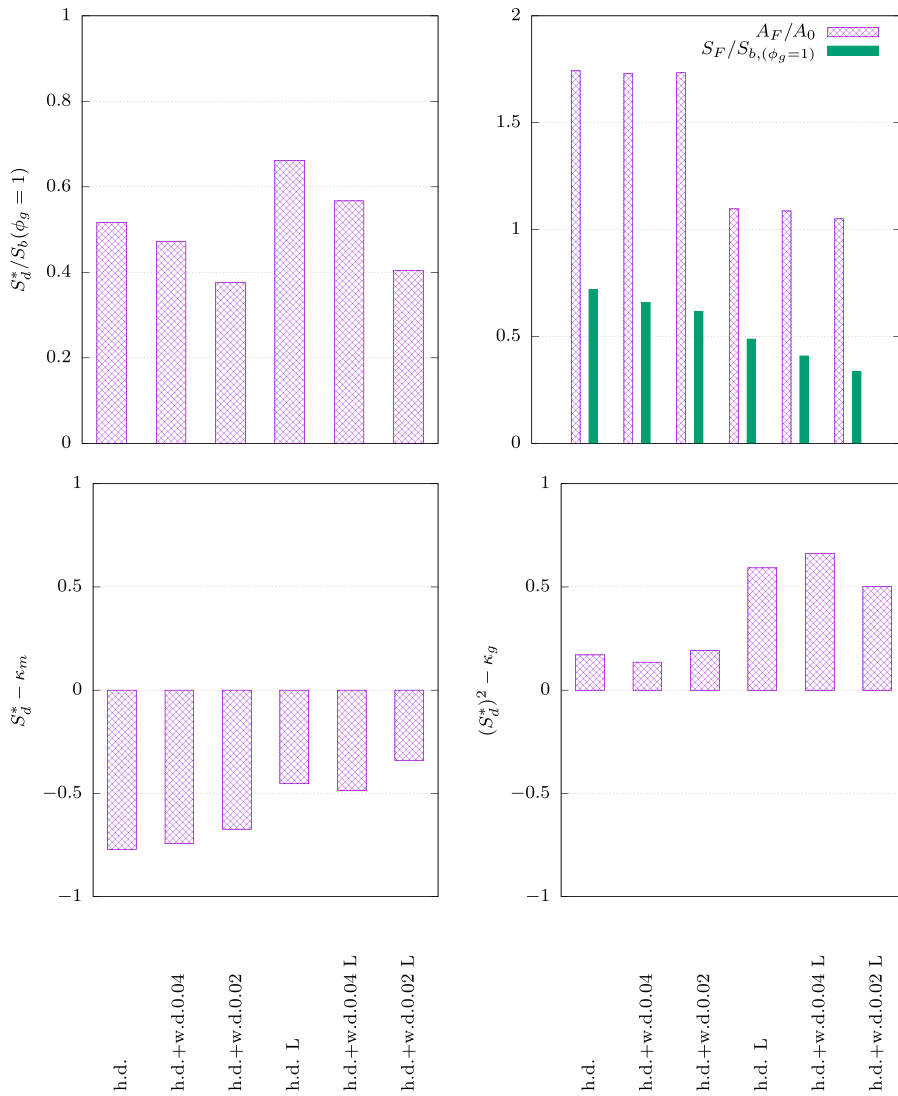
FIG. 7. Variations of (top-left) mean value of $S_d^*/S_{b,(\phi_g=1)}$ for the region given by $0.1 \leq c \leq 0.9$, (top-right) $S_F/S_{b,(\phi_g=1)}$ and A_F/A_0, correlation coefficients between (bottom-left) S_d^* and κ_m and (bottom-right) between S_d^{*2} and κ_g for the region given by $0.1 \leq c \leq 0.9$ for the cases considered here.

conditions. Moreover, the correlation coefficients between S_d^* and κ_m for all cases are smaller than unity in magnitude. The negative correlation between S_d^* and κ_m of c isosurfaces originates principally due to $S_t^* = -2\rho D\kappa_m/\rho_0$ and the non-linearity, reflected in the correlation coefficient being smaller than unity in magnitude, is introduced by the curvature dependences of S_r^* and S_n^* as a result of the variations of $\dot{w}_c$ and $|\nabla c|$ with curvature κ_m.[19,21,22] It was demonstrated by Peters[34] by scaling arguments that the relative importance of the S_t^* contribution toward S_d^* strengthens with increasing Karlovitz number, and thus, the correlation coefficients between S_d^* and κ_m in the turbulent cases assume values closer to -1.0 than in the laminar cases. The non-linear curvature dependences of S_r^* and S_n^* oppose within the reaction zone and therefore partially nullify each other.[52–54] Hence, the non-linearity of the curvature dependence of $(S_r^* + S_n^*)$ strengthens when the relative importance of S_r^* diminishes. As the contribution of S_r^* to S_d^* weakens with the decrease in water droplet diameter, the cases with an initial normalized water droplet diameter of $a_d/\delta_{st} = 0.02$ show

correlation coefficients deviating farther away from -1.0 than other cases because of the increased non-linear curvature dependences of $(S_r^* + S_n^*)$ for the cases with small water droplets (e.g., initial $a_d/\delta_{st} = 0.02$ water droplet cases).

Finally, it can be seen from Fig. 7 (bottom-right) that S_d^{*2} exhibits a strong positive correlation with κ_g only for the laminar cases but for others S_d^{*2} and κ_g are weakly correlated. Using $\kappa_1 = (\kappa_m + \varepsilon)$ and $\kappa_2 = (\kappa_m - \varepsilon)$ (where ε is a parameter), one gets $\kappa_g = \kappa_m^2 - \varepsilon^2$, which can be utilized to rewrite S_d^{*2} as

$$S_d^{*2} = (S_n^* + S_r^* + S_s^* + S_z^*)^2 - 2(S_n^* + S_r^* + S_s^* + S_z^*)\rho D\kappa_m/\rho_0 + 4\rho^2 D^2(\kappa_g + \varepsilon^2)/\rho_0^2. \tag{11}$$

Equation (11) allows for the analysis of the relation between the flame displacement speed and Gauss curvature and suggests that a strong positive correlation between S_d^{*2} and κ_g can only be realized when ε is small and contributions arising from $(S_n^* + S_r^* + S_s^* + S_z^*)$ to S_d^*

remain relatively weak in comparison with S_t^*. It can be seen from a comparison between Figs. 5 and 6 that the variations of κ_m and κ_g for c isosurfaces are relatively small for the laminar cases, and thus, ε is expected to be small in these cases, and therefore, this trend strengthens for small water droplet diameters (e.g., initial $a_d/\delta_{st} = 0.02$ water droplet cases). Therefore, the positive correlation between S_d^{*2} and κ_g is found to be stronger in the laminar cases than in the turbulent cases. This suggests that the magnitudes of S_d^* in either cup convex or cup concave topologies induced by fuel droplet-induced wrinkles are greater than in saddle-type topologies of the c isosurfaces for the laminar water injection cases. This aspect alongside the negative correlation between S_d^* and κ_m of the c isosurfaces suggests high positive and negative values of S_d^* are obtained at cup concave and cup convex topologies, respectively, for the laminar water droplet cases, which act to flatten the flame. However, in turbulent cases without water injection and with water injection, the cup convex or cup concave topologies are relatively more stable because of weaker positive correlation between S_d^{*2} and κ_g than those in the corresponding laminar cases. This is reflected in the decrease in the normalized flame surface area A_F/A_0 (where $A_F = \int_V |\nabla c| dV$) as a result of water injection under laminar condition but A_F/A_0 values are not appreciably affected by water injection for the turbulent cases considered here. This can be substantiated by the results shown in Fig. 7 (top-right), which also indicates that the extent of this reduction of A_F/A_0 for the laminar cases is more prevalent for the smaller water droplet diameter cases. Figure 7 (top-right) further indicates that the extent of the reduction of S_F as a result of water injection in the laminar cases is greater than the reduction of A_F. The reduction of A_F as a result of water injection contributes to the drop in S_F, but the cooling effects associated with latent heat extraction for water droplets reduce the reaction rate magnitude per unit area, which is responsible for a greater extent of the drop in S_F than that of A_F in the laminar cases considered here. The flame surface area A_F values for all turbulent cases remain comparable but the value of S_F decreases as a result of water injection. This trend strengthens

with decreasing water droplet diameter as the cooling effects associated with latent heat extraction for water droplets reduce the reaction rate magnitude per unit area in the turbulent cases considered here.

Finally, Fig. 8 depicts the PDFs of normalized reaction rate $\dot{w}_c \times \delta_{st}/\rho_0 S_{b,(\phi_g=1)}$ for turbulent (left) and laminar (right) cases. It is clearly visible that the introduction of water results in a leftward shift in the distributions, indicating a decrease in the reactivity of the system (which is more prevalent for smaller droplets), consistent with the findings presented in Fig. 7.

V. CONCLUSIONS

Carrier-phase DNS of water injection on statistically planar turbulent n-heptane spray flames (where the fuel is supplied in the form of mono-sized droplets on the unburnt gas side) has been carried out for an overall (i.e., liquid + gaseous) equivalence ratio of unity for different water, fixed fuel droplet diameters and flow conditions. It has been found that water droplets do not significantly evaporate ahead of the flame and most of the evaporation of water droplets starts to take place in the reaction zone and is completed within the burnt gas. By contrast, most fuel droplets evaporate as they approach the flame and continue to evaporate within the flame although some droplets can survive until the burnt gas side is reached. This difference in evaporation behavior between water and fuel droplets occurs because of the much greater latent heat of water than n-heptane. However, the finite rate of evaporation of fuel droplets leads to predominantly fuel–lean combustion within the gaseous phase although the overall equivalence ratio remains equal to unity. The probability of finding a fuel–lean mixture increases under turbulent conditions because the evaporated fuel vapor gets transported away more easily from the evaporation sites due to turbulent fluid motion. It has been found that the flame curvature variation and the probabilities of obtaining cup convex and cup concave topologies induced by fuel droplet-induced flame wrinkles in laminar cases decrease with water injection and this effect is particularly strong for small values of water droplet diameter. However, these effects are eclipsed by flow-induced flame wrinkling in turbulent cases
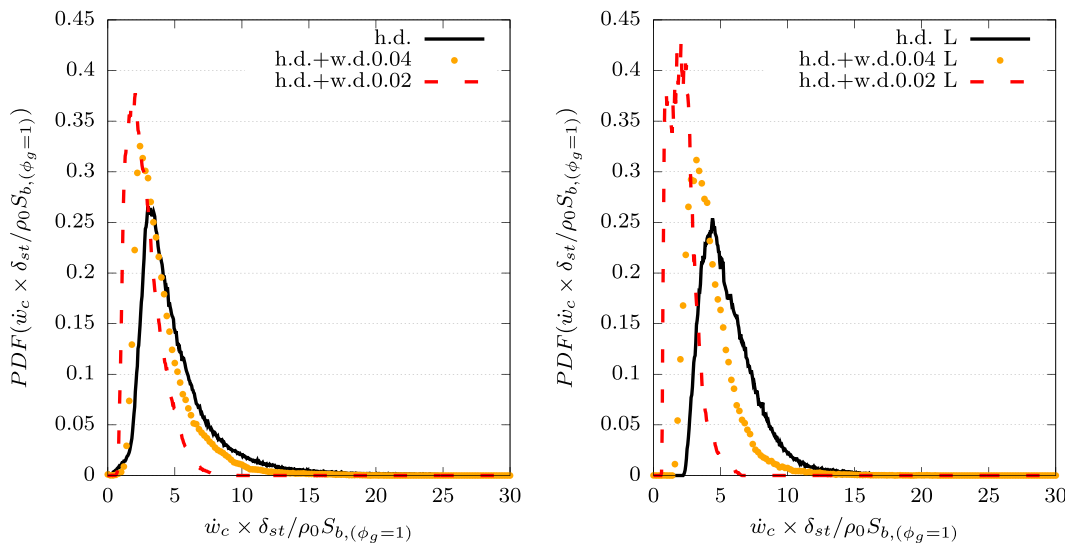

FIG. 8. PDFs of reaction rate $\dot{w}_c$ in the domain portion $0.7 \leq c \leq 0.9$ for initial turbulence intensity of $u'/S_{b,(\phi_g=1)} = 4.0$ (left) and laminar (right). The statistics are taken at $t = 4.0t_{chem}$.

where curvature variation has not been found to be affected significantly by water injection. The higher rate of evaporation and the associated latent heat extraction for smaller water droplets induce stronger cooling effects, which act to weaken the effects of chemical reaction. This is reflected in the decreases of mean values of density-weighted displacement speed with decreasing water droplet diameter. Moreover, it has been found that the negative correlation coefficient between the density-weighted displacement speed S_d^* and curvature κ_m decreases in magnitude with decreasing water droplet diameter. Furthermore, a strong positive correlation between S_d^{*2} and Gauss curvature κ_g is obtained for the laminar water injection cases with small water droplet diameter, which along with the negative correlation between S_d^* and κ_m, leads to the flattening of the flame surface. Thus, both the reaction rate of the reaction progress variable and flame surface area decrease with decreasing water droplet diameter in the case of water injection in the laminar cases due to the combined effects of cooling induced by the latent heat extraction and this effect is aided by the flame surface flattening. This is reflected in the decrease in the volume-integrated burning rate with decreasing water droplet diameter, and its reduction as a result of water injection is greater than the drop in flame surface area. By contrast, flame surface area for all turbulent cases remains comparable, and thus, the drop in the reaction rate magnitude per unit area is principally responsible for the decreasing trend of the volume-integrated burning rate with decreasing water droplet diameter in the turbulent cases considered here. Although the qualitative nature of the findings of the current analysis is expected to be independent of the choice of the chemical mechanism, the present results will need to be verified using detailed chemistry DNS for quantitative predictions.

ACKNOWLEDGMENTS

AUTHOR DECLARATIONS
Conflict of Interest

The authors have no conflicts to disclose.

Author Contributions

Riccardo Concetti: Conceptualization (equal); Data curation (lead); Formal analysis (lead); Writing – review & editing (equal). **Josef Hasslberger:** Conceptualization (equal); Supervision (equal); Writing – review & editing (equal). **Nilanjan Chakraborty:** Conceptualization (equal); Supervision (equal); Writing – original draft (equal). **Markus Klein:** Conceptualization (equal); Supervision (equal); Writing – review & editing (equal).

DATA AVAILABILITY

The data that support the findings of this study are available from the corresponding author upon reasonable request.

REFERENCES

[1] G. Thomas, A. Jones, and M. Edwards, "Influence of water sprays on explosion development in fuel-air mixtures," Combust. Sci. Technol. **80**, 47–61 (1991).

[2] G. Thomas, "On the conditions required for explosion mitigation by water sprays," Process Saf. Environ. Prot. **78**, 339–354 (2000).

[3] P. Zhang, Y. Zhou, X. Cao, X. Gao, and M. Bi, "Mitigation of methane/air explosion in a closed vessel by ultrafine water fog," Saf. Sci. **62**, 1–7 (2014).

[4] S. Lellek, "Pollutant formation in premixed natural gas swirl flames with water injection," Ph.D. thesis (Technische Universität München, 2017).

[5] Y. B. Zeldvich, "The oxidation of nitrogen in combustion and explosions," J. Acta Physicochim. **21**, 577 (1946).

[6] P. Zhang, Y. Zhou, X. Cao, X. Gao, and M. Bi, "Enhancement effects of methane/air explosion caused by water spraying in a sealed vessel," J. Loss Prev. Process Ind. **29**, 313–318 (2014).

[7] K. Van Wingerden and B. Wilkins, "The influence of water sprays on gas explosions. Part 1: Water-spray-generated turbulence," J. Loss Prev. Process Ind. **8**, 53–59 (1995).

[8] C. Nicoli, P. Haldenwang, and B. Denet, "Premixed flame dynamics in presence of mist," Combust. Sci. Technol. **191**, 197–207 (2019).

[9] J. Hasslberger, G. Ozel-Erol, N. Chakraborty, M. Klein, and S. Cant, "Physical effects of water droplets interacting with turbulent premixed flames: A direct numerical simulation analysis," Combust. Flame **229**, 111404 (2021).

[10] G. Koroll and S. Mulpuru, "The effect of dilution with steam on the burning velocity and structure of premixed hydrogen flames," in *Symposium (International) on Combustion* (Elsevier, 1988), Vol. 21, pp. 1811–1819.

[11] G. Koroll, R. Kumar, and E. Bowles, "Burning velocities of hydrogen-air mixtures," Combust. Flame **94**, 330–340 (1993).

[12] C. Dopazo, J. Martín, and J. Hierro, "Local geometry of isoscalar surfaces," Phys. Rev. E **76**, 056316 (2007).

[13] F. Zhang, T. Zirwes, P. Habisreuther, and H. Bockhorn, "Effect of unsteady stretching on the flame local dynamics," Combust. Flame **175**, 170–179 (2017).

[14] T. Zirwes, F. Zhang, Y. Wang, P. Habisreuther, J. A. Denev, Z. Chen, H. Bockhorn, and D. Trimis, "In-situ flame particle tracking based on barycentric coordinates for studying local flame dynamics in pulsating Bunsen flames," Proc. Combust. Inst. **38**, 2057–2066 (2021a).

[15] T. Zirwes, F. Zhang, and H. Bockhorn, "Memory effects of local flame dynamics in turbulent premixed flames," Proc. Combust. Inst. **39**, 2349–2358 (2023).

[16] R. Concetti, J. Hasslberger, N. Chakraborty, and M. Klein, "Analysis of water droplet interaction with turbulent premixed and spray flames using carrier phase direct numerical simulations," Combust. Sci. Technol. **195**, 1411–1433 (2023).

[17] N. Chakraborty and R. S. Cant, "A priori analysis of the curvature and propagation terms of the flame surface density transport equation for large eddy simulation," Phys. Fluids **19**, 105101 (2007).

[18] N. Chakraborty, M. Champion, A. Mura, and N. Swaminathan, "Scalar dissipation rate approach to reaction rate closure," in *Turbulent Premixed Flames* (Cambridge University Press, 2011).

[19] D. H. Wacks, N. Chakraborty, and E. Mastorakos, "Statistical analysis of turbulent flame-droplet interaction: A direct numerical simulation study," Flow. Turbul. Combust. **96**, 573–607 (2016).

[20] G. Ozel Erol, J. Hasslberger, M. Klein, and N. Chakraborty, "A direct numerical simulation investigation of spherically expanding flames propagating in fuel droplet-mists for different droplet diameters and overall equivalence ratios," Combust. Sci. Technol. **191**, 833–867 (2019a).

[21] G. Ozel Erol, J. Hasslberger, M. Klein, and N. Chakraborty, "Propagation of spherically expanding turbulent flames into fuel droplet-mists," Flow. Turbul. Combust. **103**, 913–941 (2019b).

[22] G. Ozel-Erol, J. Hasslberger, M. Klein, and N. Chakraborty, "A direct numerical simulation analysis of turbulent V-shaped flames propagating into droplet-laden mixtures," Int. J. Multiphase Flow **133**, 103455 (2020).

[23] G. Ozel-Erol, J. Hasslberger, N. Chakraborty, and M. Klein, "Effects of water droplet injection on turbulent premixed flame propagation: A direct numerical simulation investigation," Flow. Turbul. Combust. **110**, 105–123 (2023).

[24] C. Rutland and A. Trouvé, "Direct simulations of premixed turbulent flames with nonunity Lewis numbers," Combust. Flame **94**, 41–57 (1993).

[25] E. Fernández-Tarrazo, A. L. Sánchez, A. Liñán, and F. A. Williams, "A simple one-step chemistry model for partially premixed hydrocarbon combustion," Combust. Flame **147**, 32–38 (2006).

[26] M. Chaos, A. Kazakov, Z. Zhao, and F. L. Dryer, "A high-temperature chemical kinetic model for primary reference fuels," Int. J. Chem. Kinetics **39**, 399–414 (2007).

[27] J. Réveillon and L. Vervisch, "Spray vaporization in nonpremixed turbulent combustion modeling: A single droplet model," Combust. Flame **121**, 75–90 (2000).

[28] Y. Wang and C. Rutland, "Effects of temperature and equivalence ratio on the ignition of *n*-heptane fuel spray in turbulent flow," Proc. Combust. Inst. **30**, 893–900 (2005).

[29] A. P. Wandel, N. Chakraborty, and E. Mastorakos, "Direct numerical simulations of turbulent flame expansion in fine sprays," Proc. Combust. Inst. **32**, 2283–2290 (2009).

[30] A. Neophytou, E. Mastorakos, and R. Cant, "DNS of spark ignition and edge flame propagation in turbulent droplet-laden mixing layers," Combust. Flame **157**, 1071–1086 (2010).

[31] C. T. Crowe, J. D. Schwarzkopf, M. Sommerfeld, and Y. Tsuji, *Multiphase Flows with Droplets and Particles* (CRC Press, 2011).

[32] K. K. Kuo, *Principles of Combustion* (John Wiley & Sons, New York, 1986).

[33] A. Fujita, H. Watanabe, R. Kurose, and S. Komori, "Two-dimensional direct numerical simulation of spray flames—Part 1: Effects of equivalence ratio, fuel droplet size and radiation, and validity of flamelet model," Fuel **104**, 515–525 (2013).

[34] N. Peters, *Turbulent Combustion* (Cambridge University Press, 2000).

[35] T. Echekki and J. H. Chen, "Structure and propagation of methanol–air triple flames," Combust. Flame **114**, 231–245 (1998).

[36] H. G. Im and J. H. Chen, "Structure and propagation of triple flames in partially premixed hydrogen–air mixtures," Combust. Flame **119**, 436–454 (1999).

[37] H. G. Im and J. H. Chen, "Effects of flow strain on triple flame propagation," Combust. Flame **126**, 1384–1392 (2001).

[38] J. H. Chen, E. R. Hawkes, R. Sankaran, S. D. Mason, and H. G. Im, "Direct numerical simulation of ignition front propagation in a constant volume with temperature inhomogeneities: I. Fundamental analysis and diagnostics," Combust. Flame **145**, 128–144 (2006).

[39] A. Hadadpour, S. Xu, Y. Zhang, X.-S. Bai, and M. Jangi, "An extended FGM model with transported PDF for LES of spray combustion," Proc. Combust. Inst. **39**, 4889–4898 (2023).

[40] J. A. de Swart, R. J. Bastiaans, J. A. van Oijen, L. P. H. de Goey, and R. S. Cant, "Inclusion of preferential diffusion in simulations of premixed combustion of hydrogen/methane mixtures with flamelet generated manifolds," Flow. Turbul. Combust. **85**, 473–511 (2010).

[41] T. Zirwes, F. Zhang, P. Habisreuther, M. Hansinger, H. Bockhorn, M. Pfitzner, and D. Trimis, "Identification of flame regimes in partially premixed combustion from a quasi-DNS dataset," Flow. Turbul. Combust. **106**, 373–404 (2021b).

[42] M. Hansinger, T. Zirwes, J. Zips, M. Pfitzner, F. Zhang, P. Habisreuther, and H. Bockhorn, "The Eulerian stochastic fields method applied to large eddy simulations of a piloted flame with inhomogeneous inlet," Flow. Turbul. Combust. **105**, 837–867 (2020).

[43] M. Lawes and A. Saat, "Burning rates of turbulent iso-octane aerosol mixtures in spherical flame explosions," Proc. Combust. Inst. **33**, 2047–2054 (2011).

[44] S. Hayashi, S. Kumagai, and T. Sakai, "Propagation velocity and structure of flames in droplet-vapor-air mixtures," Combust. Sci. Technol. **15**, 169–177 (1977).

[45] T. J. Poinsot and S. Lele, "Boundary conditions for direct simulations of compressible viscous flows," J. Comput. Phys. **101**, 104–129 (1992).

[46] P. Schroll, A. P. Wandel, R. S. Cant, and E. Mastorakos, "Direct numerical simulations of autoignition in turbulent two-phase flows," Proc. Combust. Inst. **32**, 2275–2282 (2009).

[47] G. Batchelor and A. Townsend, "Decay of turbulence in final period," Proc. R. Soc., London A **194**, 527–543 (1948).

[48] *Rotexo-Softpredict-Cosilab* (GmbH and Co. KG Bad Zwischenahn, Germany).

[49] A. Neophytou and E. Mastorakos, "Simulations of laminar flame propagation in droplet mists," Combust. Flame **156**, 1627–1640 (2009).

[50] G. Ozel Erol and N. Chakraborty, "Effects of mean inflow velocity and droplet diameter on the propagation of turbulent V-shaped flames in droplet-laden mixtures," Fluids **6**, 1 (2020).

[51] J. Hasslberger, R. Concetti, N. Chakraborty, and M. Klein, "Inertial effects on the interaction of water droplets with turbulent premixed flames: A direct numerical simulation analysis," Proc. Combust. Inst. **39**, 2575–2586 (2023).

[52] N. Peters, P. Terhoeven, J. H. Chen, and T. Echekki, "Statistics of flame displacement speeds from computations of 2-D unsteady methane-air flames," in *Symposium (International) on Combustion* (Elsevier, 1998), Vol. 27, pp. 833–839.

[53] T. Echekki and J. H. Chen, "Analysis of the contribution of curvature to premixed flame propagation," Combust. Flame **118**, 308–311 (1999).

[54] F. Keil, M. Amzehnhoff, U. Ahmed, N. Chakraborty, and M. Klein, "Comparison of flame propagation statistics extracted from DNS based on simple and detailed chemistry—Part 1: Fundamental flame turbulence interaction," Energies **14**, 5548 (2021).

22 July 2024 10:33:30